TOPOGRAPHIC DISTRIBUTION OF SNOW WATER EQUIVALENT IN THE SIERRA NEVADA

Karl Rittger[1], Annelen Kahl[1] and Jeff Dozier[1]

ABSTRACT

Water supply forecasts in the Sierra Nevada using ground-based measurements of snow water equivalent (SWE) are uncertain because neither point measurements nor transects adequately explain spatial or temporal variability in mountainous terrain. To address this problem, we combine satellite-based retrievals of fractional snow cover in 2006 with energy balance calculations to reconstruct the SWE values throughout the melt season. Model estimates when compared to snow pillows at maximum accumulation are unbiased and have an RMS error of 297 to 417 mm. We compare this retrospective calculation of distributed SWE with two real-time models: (i) interpolation from pillows, courses, and satellite snow cover, and (ii) the Snow Data Assimilation System (SNODAS). The interpolation and SNODAS models show complete melt out more than a month earlier than reconstruction, and their total SWE volumes are 68% and 87% of the reconstructed volume. At elevations below 1500 m, the reconstruction model has less total SWE because of early season melt. Above 3000 m, the reconstruction shows more SWE than the real time models, which depend on surface measurements that do not sample the higher elevations. The results indicate that spatial patterns from the reconstruction could improve estimates of snow accumulation and duration. (KEYWORDS: snow-covered area, snow water equivalent, energy balance, MODIS)

INTRODUCTION

In the Sierra Nevada most streamflow comes from snow, and our reservoirs hold only a little more than average annual snowmelt runoff. Point measurements from snow pillows and transects from snow courses remain the primary source of data about snow, but those data do not correctly explain spatial and temporal variability in mountainous terrain. Significant areas of the Sierra Nevada lie above the highest snow pillows and courses, and neither moderate nor steep slopes are monitored. If water managers better understood the distribution of snow and its melt, they could better deal with competing priorities for flood protection and resource use for cities, industries, agriculture, hydropower, and ecosystems.

Two separate entities, the NOAA/NWS California Nevada River Forecast Center (CNRFC) and the California Department of Water Resources (CADWR), work together but produce their own estimates of streamflow (CADWR, 2011; NOAA/NWS, 2011). The CNRFC uses two methods to produce weekly and seasonal forecasts. The first relies on a multiple linear regression of streamflow against snow pillows and courses, and the second uses the same information along with a model to produce ensemble forecasts. The regressions do not predict the timing, an important factor given the limited capacity to store water. Historical predictions have been inaccurate in both wet and dry years, and these models use no information on snow water equivalent (SWE) at high elevations. Decreasing snow accumulation across the western US (Mote et al., 2005) and earlier snowmelt runoff in California (Maurer et al., 2007) make forecasting a challenging problem because the statistical environment is not stationary (Milly et al., 2008). Projected changes in runoff during the lifetime of major water infrastructure are large enough to exceed the range of historical behaviors (Seager et al., 2007); therefore a more mechanistic way of estimating snowmelt and streamflow is needed.

Spatial interpolation or models such as SNODAS (Barrett, 2003) can estimate spatially distributed SWE throughout the season. Reconstruction models are, by definition, retrospective, because they use satellite-derived information about snow-cover depletion that is not available to the real-time methods. Reconstruction's utility is its lack of reliance on ground measurements and, therefore, its independent estimates that can be used to evaluate real-time models and to better understand the topographic distribution of snow.

Paper presented Western Snow Conference 2011

[1] Karl Rittger, Bren School of Environmental Science & Management, University of California, Santa Barbara, CA 93106-5131, krittger@bren.ucsb.edu

[1] Annelen Kahl, Bren School of Environmental Science & Management, University of California, Santa Barbara, CA 93106-5131, akahl@bren.ucsb.edu

[1] Jeff Dozier, Bren School of Environmental Science & Management, University of California, Santa Barbara, CA 93106-5131, dozier@bren.ucsb.edu

STUDY AREA

The Sierra Nevada maritime snowpack encompasses 4 major regions: Sacramento, San Joaquin, Tulare and Eastern Sierra (Figure 1). The thin black lines show the hydrologic unit code 8 (HUC8) basins at which water is managed. The total area of all basins is 111,000 km^2. The 4 regions range in area from 13,000 to 24,000 km^2, and the HUC8 basins range in area from 1000-4000 km^2. Figure 1 also shows locations of snow pillows and snow courses.

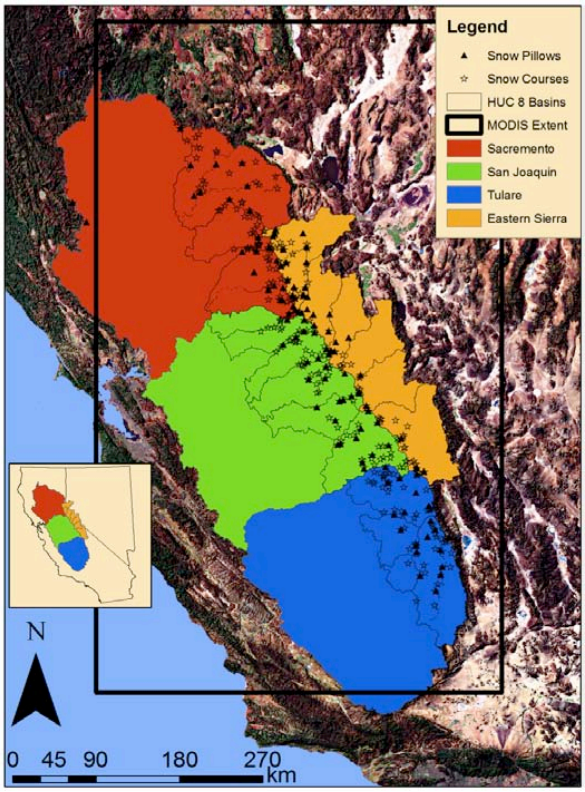

Figure 1. Sierra Nevada study region, HUC8 basins, snow pillow and snow course measurements, and bounding box for the MODIS data used.

Basins in the San Joaquin drainage generally have higher elevations than those in the Sacramento or Tulare, while Eastern Sierra basins have the highest elevations but lie on the lee side of the range. Basins in the Sacramento, San Joaquin and Tulare regions are oriented toward the southwest, with the exception of the Kern which flows southward, while the Eastern Sierra basins are oriented northeast. The forest canopy decreases from north to south in the Sacramento, San Joaquin and Tulare drainages, as bare soils and shrubs replace forests. The Sacramento region is the most highly instrumented, providing more locations for validation, while the Eastern Sierra is the least instrumented.

SPATIAL ESTIMATES OF SNOW WATER EQUIVALENT

In this section, we first describe the MODSCAG model for remote sensing of snow-covered area and albedo. Then we describe three ways of independently estimating spatially distributed snow water equivalent: a simple real-time interpolation, the more sophisticated real-time SNODAS model, and, in more detail, the retrospective reconstruction model. MODSCAG is used in both the interpolation and reconstruction models.

Snow cover and albedo

Snow covered area and grain size are derived from data from the Moderate Resolution Imaging Spectroradiometer (MODIS) using the MODSCAG model (MODIS snow-covered area and grain size: Painter et al., 2009). This algorithm combines atmospherically corrected surface reflectance estimates (MODIS product MOD09GA) with spectral mixture analysis to determine the fraction of each 500 m pixel covered with snow, along with its grain size. The albedo of pure snow is fit to an empirical relationship with grain size and illumination angle. The MOD09GA reflectance data have gaps and errors because of cloud cover and sensor viewing geometry, so we use the daily time series with a combination of noise filtering, snow/cloud discrimination, interpolation and smoothing to produce our best estimate of daily snow cover and albedo (Dozier et al., 2008). Finally, we adjust the satellite-observed snow cover for under-canopy snow (Molotch and Margulis, 2008) by each pixel's vegetation cover at the annual 10th percentile ($f_{VEG,Minimum}$), thereby accounting for forests and for shrubs and grass that are uncovered as the snow recedes.

$$f_{SCA} = \frac{f_{SCA\ viewable}}{1 - f_{VEG,Miminum}} \quad (1)$$

Figure 2 shows the viewable snow covered area ($f_{SCA\ viewable}$) and the canopy corrected snow covered area (f_{SCA}) for the first of each month from March through August 2006.

Interpolation of Snow Water Equivalent

The interpolation combines smoothed fractional snow cover at 500 m resolution (Dozier et al., 2008) with data from snow courses and snow pillows (Figure 1). The in situ SWE data come from the California Data Exchange Center (CADWR, 2011) and were cleaned of spurious values and other noise before being used in the interpolation. Voronoi regions (a multi-dimensional extension of Thiessen polygons) are defined in 3-dimensional

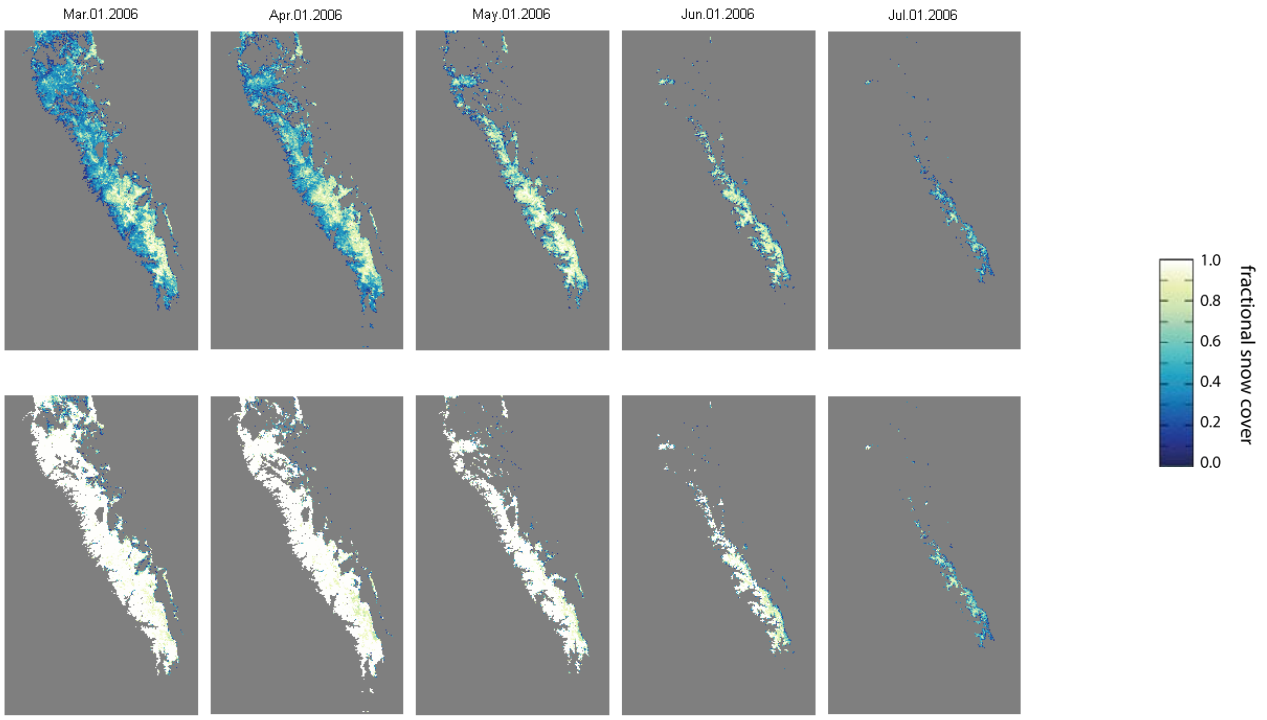

Figure 2. First of each month viewable snow-covered area (top) and canopy corrected snow-covered area (bottom).

space for each HUC8 river basin and used to select the courses and pillows used for the interpolation (Barber et al., 1996). The model does not include an orographic extrapolation of SWE above in situ observations. The interpolation estimates SWE at each grid location for a specified elevation. A spline interpolation is then fitted in the time dimension to give spatial SWE at each time step. Total SWE is constrained by fractional snow cover and tapered near the snow line to produce a more physically realistic snowpack.

Snow Data Assimilation System (SNODAS) Snow Water Equivalent

The NOAA National Weather Service's National Operational Hydrologic Remote Sensing Center (NOHRSC) Snow Data Assimilation System (SNODAS) provides estimates of snow cover and associated variables to support hydrologic modeling and analysis (Barrett, 2003). The model runs at 1 km spatial resolution and 1 hr temporal resolution for the conterminous United States and relies on satellite-derived, airborne, and ground-based observations of snow covered area and SWE. The satellite-derived snow covered area is from NOAA's Advanced Very High Resolution Radiometer (AVHRR) at 1.1 km resolution.

Reconstruction of Snow Water Equivalent

First implemented by Martinec and Rango (1981), "reconstruction" combines the satellite-derived snow cover depletion record with a calculation of the melt rate to retroactively estimate how much snow had existed at every pixel. The technique has been validated in the Sierra Nevada (Cline et al., 1998) and applied to large basins at multiple scales (Molotch and Margulis, 2008). We build on this work and apply their method to model SWE for the entire Sierra Nevada using a snowmelt model that combines both energy balance and temperature index methods. The following equation is the basis for the reconstruction:

$$SWE_N = SWE_0 - \sum_{j=1}^{N} M_j \tag{2}$$

where SWE_0 is the initial SWE, typically at seasonal maximum, SWE_N is the SWE after a series of N melt time steps M_j, and where

$$M_j = M_{P,j} \times f_{SCA,j} \tag{3}$$

$M_{P,j}$ is the potential melt at time step j and $f_{SCA,j}$ is the fractional snow-covered area at time step j. $M_{P,j}$ is calculated with a combined energy balance, temperature index model:

$$M_{P,j} = m_Q R_d + \beta_r T_d \quad (4)$$

where m_Q is a conversion factor from energy to melt, R_d is the mean net daily radiation, β_r is a degree day factor, and T_d is the mean daily temperature above 0°C. For β_r we use values from the literature (Brubaker et al., 1996; Molotch and Margulis, 2008).

Air Temperature - The reconstruction relies on a digital elevation model at 1 arc sec resolution from the Shuttle Radar Topography Mission (SRTM) that has an absolute height error of less than 16 m (Farr et al., 2007). The dual radar method is unable to determine elevations in extreme topography, mostly steep river channels, and these holes in the data are filled with elevations from the National Elevation Dataset (Gesch et al., 2002). The merged SRTM/NED elevations are resampled to 100 m. Air temperature T_A was downscaled from 1/8° NLDAS2 reanalysis data (Cosgrove et al., 2003) to 100 m grid cells using an environmental lapse rate of -6.5°C/km. The elevation difference between the coarse digital elevation model in NLDAS2 and the combined SRTM/NED digital elevation model is used to adjust the temperature. In the reconstruction model, the mean daily temperature is calculated for each pixel.

Radiation - Net shortwave (solar) radiation Q_{ns} is the difference between incoming and outgoing shortwave radiation $S_\downarrow$ and $S_\uparrow$. Incoming solar radiation $S_\downarrow$ is comprised of beam $B_{S\downarrow}$ and diffuse $D_{S\downarrow}$ radiation from the sun, and reflected radiation $R_{T\downarrow}$ from surrounding topography. Topography affects these fluxes because of variation in illumination angle and shadowing from local horizons. Incoming solar radiation on a horizontal surface from NLDAS2 (Dubayah, 1992; Cosgrove et al., 2003) is partitioned into $B_{S\downarrow}$ and $D_{S\downarrow}$ using transmittance T, exoatmospheric solar radiation S_0 and μ_0, the cosine of the solar zenith angle. Transmittance T is:

$$T = \frac{S_\downarrow}{\mu_0 S_0} \quad (5)$$

The partitioning formula (Erbs et al., 1982) has been modified for mountainous terrain (Olyphant, 1984) and uses distinctive relationships between $S_\downarrow$ and T to determine the beam and diffuse irradiance for cloud, partly cloudy and clear days. Figure 3a shows $S_\downarrow$ for April 1st.

Both the incoming beam $B_{S\downarrow}$ and diffuse $D_{S\downarrow}$ solar radiation can be approximated with a spatially averaged beam $\overline{B_{x\downarrow}}$ and diffuse downwelling $\overline{F_{x\downarrow}}$ flux centered on grid cell x and then adjusted to elevation z (Dubayah and Loechel, 1997) and corrected with a sky view factor V_d (Dozier and Frew, 1990). θ_i is the solar illumination angle on the slope and δ is a binary shadowing mask:

$$B_{S\downarrow} = \delta \cos\theta_i \overline{B_{x\downarrow}}(z) \quad (6)$$

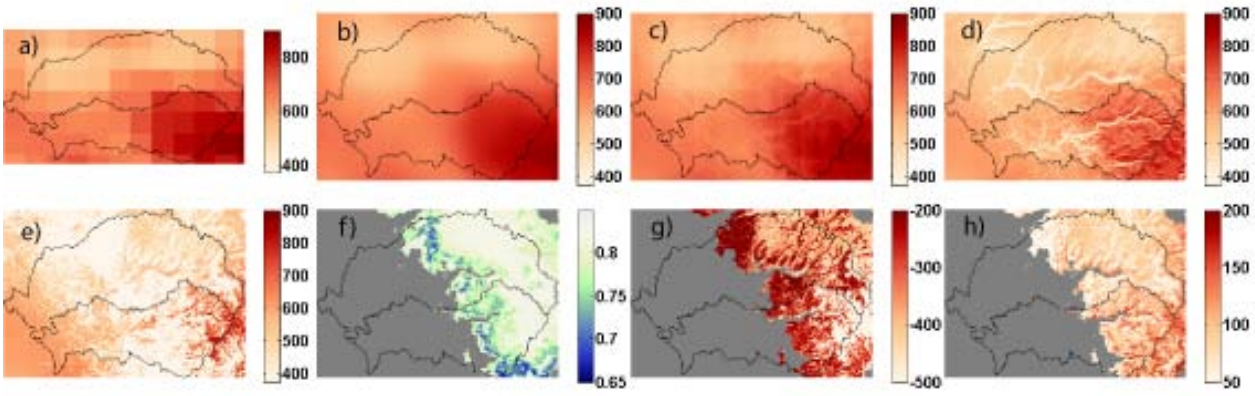

Figure 3. Shortwave radiation in the Tuolumne-Merced River basins for April 1, 2006 noon, all at 100 m resolution except (a) 1/8° NLDAS2 incoming; (b) incoming spatially integrated; (c) incoming corrected for elevation; (d) incoming corrected for topography; (e) incoming corrected for vegetation; (f) snow albedo; (g) outgoing; (h) net.

$$D_{S\downarrow} = \overline{F_{x\downarrow}}(z)V_d \quad (7)$$

We estimate both $\overline{B_{x\downarrow}}$ and $\overline{F_{x\downarrow}}$ by spatially averaging the partitioned NLDAS incoming radiation in a neighborhood centered on the 100 m SRTM/NED DEM with a Gaussian filter and a 40 km neighborhood. Daily sums for April 1st are shown in Figure 3b. Optical depths τ_0 at the NLDAS grid cell elevation and earth-sun distance R_v (in astronomical units) are derived from $\overline{B_{x\downarrow}}$ using the atmospheric airmass a including refraction (Kasten and Young, 1989):

$$\tau_0 = -a^{-1}\ln\left(\frac{\overline{B_{x\downarrow}}{R_v}^2}{\mu_0 S_0}\right) \quad (8)$$

The correction for airmass uses temperature and pressure. Temperature was downscaled from 1/8° using a standard environmental lapse rate. NLDAS2 pressure was downscaled with the hydrostatic equation and density. Then the optical depth τ_z at elevation z is estimated assuming a pressure-dependent decrease in direct transmittance; the elevation-corrected solar radiation is:

$$B_{z\downarrow} = \mu_0 S_0 e^{-a\tau_z} \quad (9)$$

The diffuse irradiance $F_{z\downarrow}$ at elevation z is obtained from an empirical formulation (Dubayah, 1992). M_0 and M_z are empirical factors representing the unabsorbed fluxes at reference elevation z_0 and elevation z:

$$F_{z\downarrow} = F_{z_0\downarrow}\frac{M_z - e^{-\tau_z/\mu_0}}{M_0 - e^{-\tau_0/\mu_0}} \quad (10)$$

$$M_z = \left(1 - 0.027e^{2P_z/P_0}\right)\left[1.075 - 0.105\ln\left({}^1/_{\mu_0}\right)\right] \quad (11)$$

Figure 3c and d show the elevation corrected and topographically corrected incoming solar radiation.

We then adjust the topographically corrected diffuse and beam components for vegetation using separate transmissivity values for beam and diffuse irradiance (Link and Marks, 1999; Garen and Marks, 2005). Figure 3e shows the vegetation-corrected values.

Reflected radiation depends on the broadband surface albedo α. Spatially varying albedo (Figure 3f) from MODSCAG was used to estimate the reflected radiation (Figure 3g) and the net solar radiation Q_{ns} (Figure 3h).

Longwave Radiation - Net longwave radiation Q_{nl} for a horizontal surface is comprised of incoming radiation from the atmosphere $L_{A\downarrow}$, incoming radiation from the surrounding terrain $L_{T\downarrow}$, and outgoing radiation from the surface $L_{S\uparrow}$:

$$Q_{nl} = L_A\downarrow + L_T\downarrow - L_S\uparrow \quad (12)$$

Here we ignore the contribution for the surrounding terrain. Future efforts could include this contribution to incoming longwave by using MODIS-derived land-surface temperature (Wan and Dozier, 1996).

$L_{A\downarrow}$ is the radiation emitted by the atmosphere, which can be modeled as a gray body with an effective atmospheric emissivity ε_A and air temperature T_A (Marks and Dozier, 1979):

$$L_{A\downarrow} = \varepsilon_A \sigma T_A^4 \ (\sigma \text{ is the Stefan-Boltzmann constant}) \quad (13)$$

Using $L_{A\downarrow}$ (Figure 4a) along with T_A from NLDAS2, we can estimate ε_A for each 1/8° grid cell (Figure 4b). ε_A is spatially integrated using a Gaussian moving average filter to account for time-integrated estimates of ε_A (Figure 4c). Next, $L_{A\downarrow}$ at 100 m (Figure 4d) is estimated using equation (13), the 100 m downscaled T_A and assuming ε_A is constant over each 1/8° grid cell (Molotch and Margulis, 2008).

Slopes are accounted for using parameters developed for mountainous terrain: the sky view factor V_d and the terrain configuration factor C_t (Dozier and Frew, 1990). The snow emissivity, ε_S is assumed to be 0.99 and T_S is the surface temperature of the snow. $L_{A\downarrow}$ (Figure 4e) and $L_{T\downarrow}$ are:

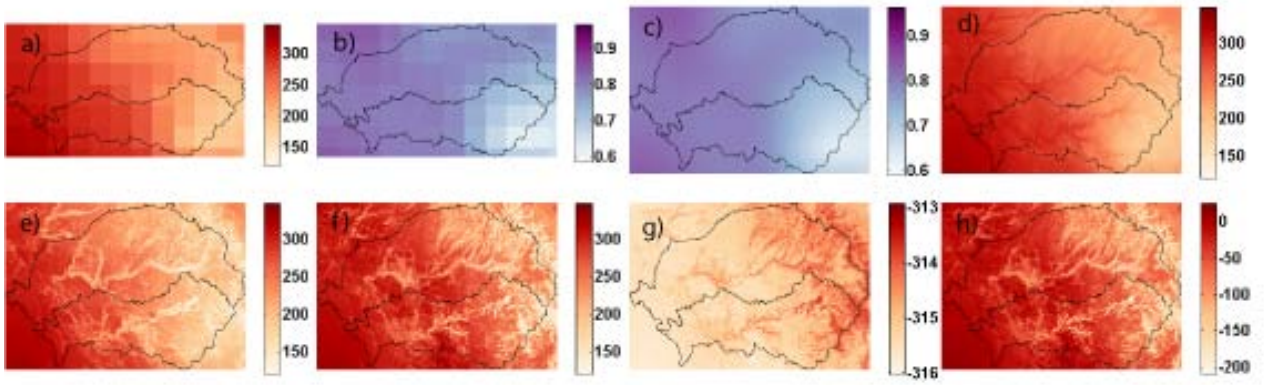

Figure 4: Longwave radiation in the Tuolumne-Merced River basins for April 1, 2006 noon. (a) 1/8° NLDAS2 incoming; (b) 1/8° $\varepsilon_{a,}$ incoming; (c) 100 m incoming spatially integrated; (d) 100 m incoming corrected for elevation; (e) 100 m incoming corrected for topography; (f) 100 m incoming corrected for vegetation; (g) 100 m outgoing; (h) 100 m net.

$$L_{A\downarrow} + L_{T\downarrow} = (\varepsilon_A T_A^4) V_d + (\varepsilon_S T_S^4) C_t \quad (14)$$

In the forest, longwave radiation is corrected for vegetation using canopy tranmissivity, emissivity and temperature (Link and Marks, 1999; Garen and Marks, 2005). Figure 4f shows longwave radiation corrected for vegetation.

Outgoing radiation for snow $L_{S\uparrow}$ (Figure 4h) is the sum of emitted longwave plus the very small fraction that is reflected from the snow surface. The model does not keep track of the internal energy balance of the snowpack, so T_S needed for both $L_{T\downarrow}$ and $L_{S\uparrow}$ has to be estimated. We assume the snow surface temperature is 0°C for the reconstruction model during the melt period. To confirm this assumption, we use a distributed coupled energy mass-balance model, ISNOBAL (Marks et al., 1999) to understand how the surface temperature of the snowpack changes over the season. Using a digital elevation model with 30 m resolution, we modeled the Marble Fork of the Kaweah River basin at an hourly time step. Hourly data for March 15th, April 15th, May 15th and June 15th in water year 2006 were analyzed to determine the validity of our assumption. Average snow surface temperature was at 0°C at 41% and 77% in March and April, and 100% thereafter. This calculation indicates that our assumption is likely to lead only to small errors early in the melt season.

Validation from Snow Pillows

We validated the reconstruction model at one snow pillow in each of the four regions. The snow pillows' measurements of maximum SWE are compared to results from the reconstruction method. We calculate the root mean squared error (RMSE) and the mean absolute error (MAE) for each basin. Figure 5 shows the comparison in the Truckee, American, Tuolumne and Kern River basins that have RMSE values of 350 mm, 297 mm, 417 mm and 309 mm and MAE values of 266 mm, 226 mm, 369 mm and 280 mm respectively. A smaller difference in the RMSE and MAE for the Kern indicate fewer large errors than in the Truckee. The scatter about each 1-to-1 line shows that the estimates are unbiased.

DISTRIBUTION OF SNOW WATER EQUIVALENT

In this section we compare SWE expressed as a depth, snow water volumes, and melt out dates for the entire Sierra Nevada. Both the SWE and the distribution of the area with elevation are important in understanding the distribution of the total SWE volume. Figure 6 shows April 1st SWE for the 3 models.

Mean SWE as a Depth

Figure 7 shows the mean SWE from the 3 models from April 1st to September 31st for elevations above 1200 m. The results show a similar pattern for the interpolation and SNODAS models; SWE increases from 1200 m to 3000 m and then decreases. The retrospective reconstruction model also shows an increase in SWE to 3000 m, but the reconstructed values continue to increase to 3600 m before leveling off is followed by a slight decrease below 4200 m. The maximum SWE over all elevations for the Sierra Nevada from the interpolation, SNODAS, and reconstruction are 1215 mm and 1079 mm on April 18th and 1782 mm on April 1st respectively. The maximum SWE for each elevation in all models occurs approximately on the day of the maximum mean for all elevations

except for elevations under 1500 m. Under 1500 m, the date of maximum SWE occurs 1 month earlier. This finding indicates the reconstruction model should be run for the month of March in 2006 to account for low-elevation before April 1st.

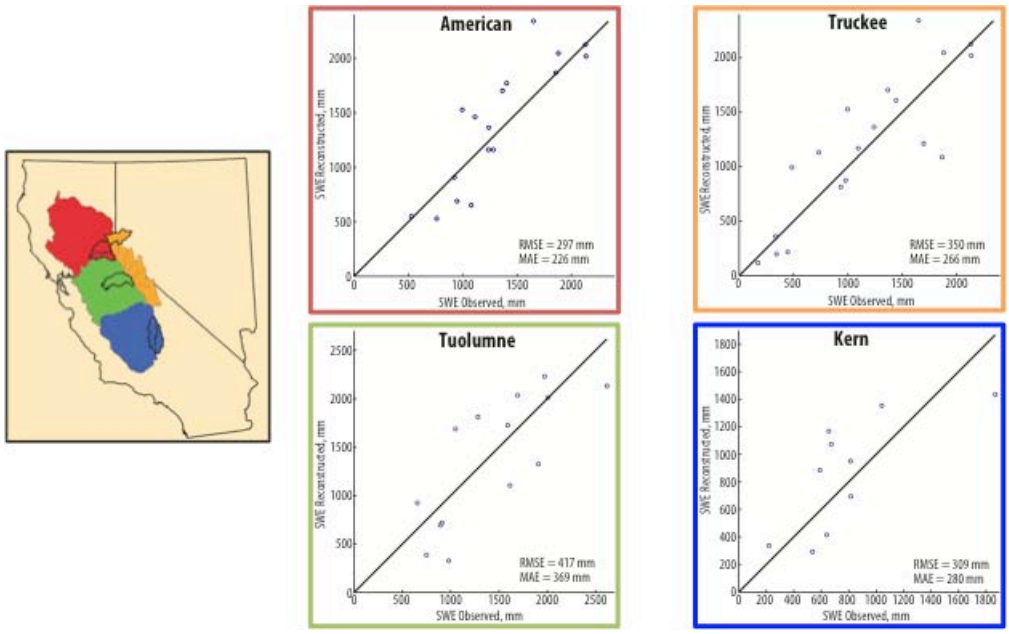

Figure 5. Comparison of reconstructed SWE to snow pillow SWE, April 1, 2006.

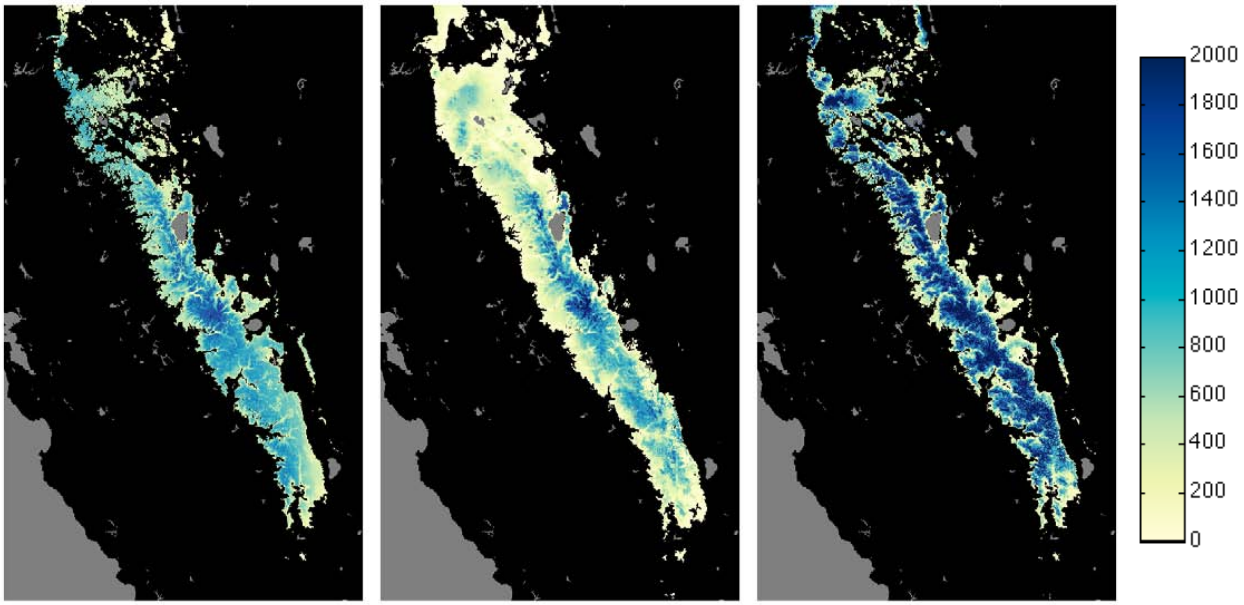

Figure 6: April 1, 2006 SWE (in mm) from interpolation (left), SNODAS (center) and reconstruction (right).

Total Snow Water Volume

We calculate the snow water volume at each elevation by multiplying the SWE by the total area at that elevation. Figure 8 shows the snow water volumes from the 3 models during April 1st to August 31st for elevations above 1200 m. The maximum volumes summed over all elevations for the Sierra Nevada are 32.9 km^3 from

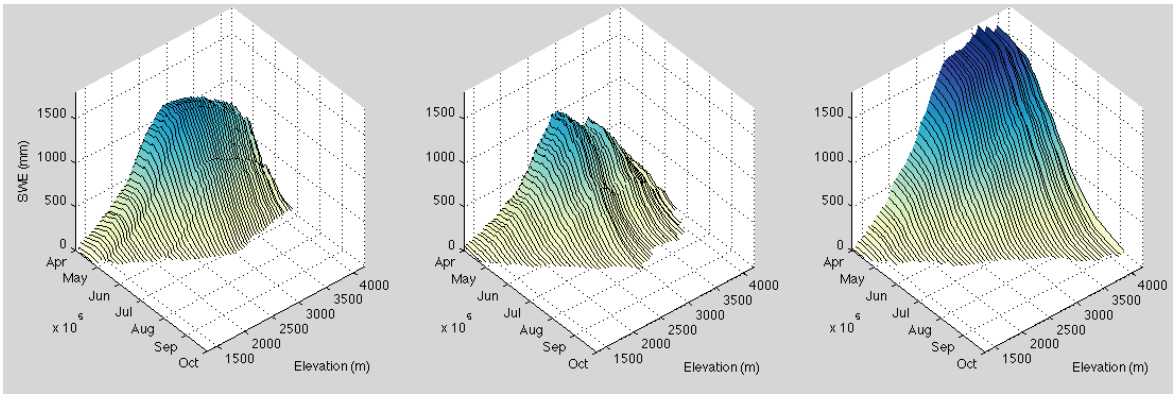

Figure 7: Mean SWE: interpolation (left), SNODAS (center) and reconstruction (right).

interpolation, 25.6 km^3 from SNODAS, and 37.9 km^3 from reconstruction. While the largest differences in SWE are at elevations above 3600 m, the largest differences in total volume are lower because the lower elevations encompass more area. The interpolation and SNODAS SWE volumes are 68% and 87% of the reconstructed volume.

Melt Out Date

SWE from the interpolation model is driven by in situ pillow and course measurements and lack observations at the highest elevations. SWE above the highest snow pillows is assumed to be the same as the data collected from these snow pillows. Therefore, when the snow pillows melt, there is nothing to interpolate. Thus data from the interpolation model becomes unreliable when snow at the pillows melts.

Melt out in Figure 7 is visible in SNODAS model around July 28th, 1 month after the melt out date from the interpolation, whereas snow at the highest elevations persists in the reconstruction model until September 5$^{th.}$ This high-elevation snow covers only a small area and does not contribute much volume to the total, thus Figure 8 shows that effective melt out for total volume occurs near August 1st for both SNODAS and the reconstruction while it occurs near July 1 for the interpolation.

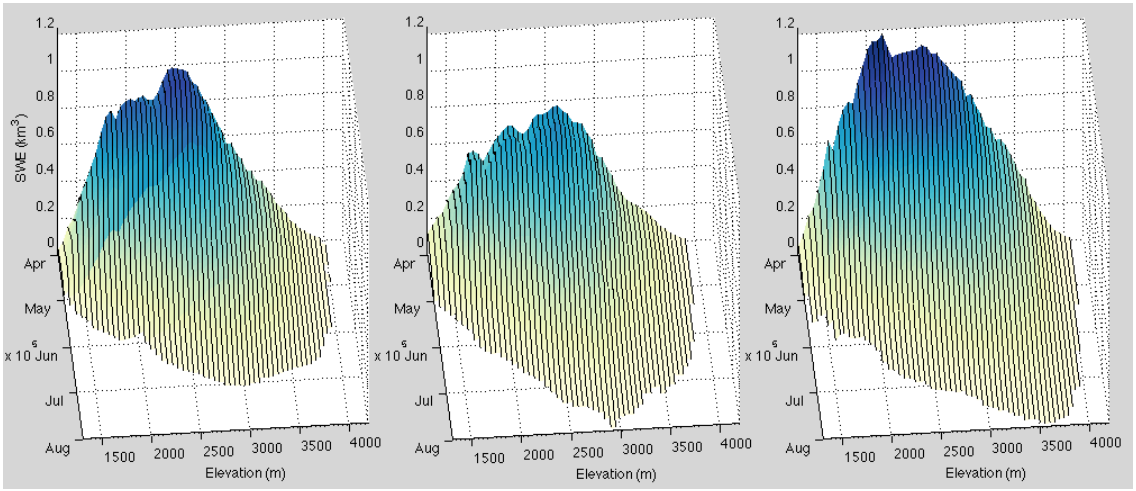

Figure 8: Snow water volume: interpolation (left), SNODAS (center) and reconstruction (right).

CONCLUSION

Understanding the spatial distribution of SWE is important to streamflow forecasting in the Sierra Nevada. SNODAS and the interpolation models can estimate spatial SWE in real time, while the reconstruction can do so only retrospectively. SNODAS and the reconstruction both take into account topography; however the reconstruction does not rely on point measurements, while SNODAS and interpolation do. When compared to snow pillows, the reconstruction method provides unbiased estimates of the topographic distribution of SWE. The method uses the snow cover record and energy balance calculations and can offer valuable information. At

elevations above snow pillows, the reconstruction provides a way to validate the real-time models and give us a better understanding of the scaling of SWE with elevation.

ACKNOWLEDGEMENTS

This work is supported by NASA Cooperative Agreement NNG04GC52A, Naval Postgraduate School Award N00244-07-1-0013, and the NASA Earth System Sciences Fellowship program.

REFERENCES

Barber, C.B., D.P. Dobkin, and H. Huhdanpaa. 1996. The quickhull algorithm for convex hulls, ACM Transactions on Mathematical Software, 22(4): 469-483, doi: 10.1145/235815.235821.

Barrett, A. 2003. National Operational Hydrologic Remote Sensing Center SNOw Data Assimiliation System (SNODAS) Products at NSIDC, Special Report 11, National Snow and Ice Data Center, Boulder.

Brubaker, K., A. Rango, and W. Kustas. 1996. Incorporating radiation inputs into the snowmelt runoff model, Hydrological Processes, 10(10): 1329-1343, doi: 10.1002/(SICI)1099-1085(199610)10:10<1329::AID-HYP464>3.0.CO;2-W.

CADWR (2011), California Data Exchange Center, http://cdec.water.ca.gov/.

Cline, D.W., R.C. Bales, and J. Dozier. 1998. Estimating the spatial distribution of snow in mountain basins using remote sensing and energy balance modeling, Water Resources Research, 34(5): 1275-1285, doi: 10.1029/97WR03755.

Cosgrove, B.A., D. Lohmann, K.E. Mitchell, P.R. Houser, E.F. Wood, J.C. Schaake, A. Robock, C. Marshall, J. Sheffield, Q.Y. Duan, L.F. Luo, R.W. Higgins, R.T. Pinker, J.D. Tarpley, and J. Meng, J. 2003. Real-time and retrospective forcing in the North American Land Data Assimilation System (NLDAS) project, Journal of Geophysical Research, 108(D22): 8842, doi: 10.1029/2002jd003118.

Dozier, J. and J. Frew. 1990. Rapid calculation of terrain parameters for radiation modeling from digital elevation data, IEEE Transactions on Geoscience and Remote Sensing, 28(5): 963-969, doi: 10.1109/36.58986.

Dozier, J., T.H. Painter, K. Rittger, and J.E. Frew. 2008. Time-space continuity of daily maps of fractional snow cover and albedo from MODIS, Advances in Water Resources, 31(11): 1515-1526, doi: 10.1016/j.advwatres.2008.08.011.

Dubayah, R. 1992. Estimating net solar radiation using Landsat Thematic Mapper and digital elevation data, Water Resources Research, 28(9): 2469-2484, doi: 10.1029/92WR00772.

Dubayah, R. and S. Loechel. 1997. Modeling topographic solar radiation using GOES data, Journal of Applied Meteorology, 36(2): 141-154, doi: 10.1175/1520-0450(1997)036<0141:MTSRUG>2.0.CO;2.

Erbs, D.G., S.A. Klein, and J.A. Duffie. 1982. Estimation of the diffuse radiation fraction for hourly, daily and monthly-average global radiation, Solar Energy, 28(4): 293-302, doi: 10.1016/0038-092X(82)90302-4.

Farr, T.G., P.A. Rosen, E. Caro, R. Crippen, R. Duren, S. Hensley, M. Kobrick, M. Paller, E. Rodriguez, L. Roth, D. Seal, S. Shaffer, J. Shimada, J. Umland, M. Werner, M. Oskin, D. Burbank, and D. Alsdorf. 2007. The Shuttle Radar Topography Mission, Reviews of Geophysics, 45(2): RG2004, doi: 10.1029/2005rg000183.

Garen, D.C., and D. Marks. 2005. Spatially distributed energy balance snowmelt modelling in a mountainous river basin: estimation of meteorological inputs and verification of model results, Journal of Hydrology, 315(1-4): 126-153, doi: 10.1016/j.jhydrol.2005.03.026.

Gesch, D., M. Oimoen, S. Greenlee, C. Nelson, M. Steuck, and D. Tyler. 2002. The National Elevation Dataset, Photogrammetric Engineering and Remote Sensing, 68(1): 5-11.

Kasten, F. and A.T. Young. 1989. Revised optical air mass tables and approximation formula, Applied Optics, 28(22): 4735-4738, doi: 10.1364/AO.28.004735.

Link, T.E. and D. Marks. 1999. Distributed simulation of snowcover mass- and energy-balance in the boreal forest, Hydrological Processes, 13(14-15): 2439-2452, doi:10.1002/(SICI)1099-1085(199910)13:14/15<2439::AID-HYP866>3.0.CO;2-1.

Marks, D. and J. Dozier. 1979. A clear-sky longwave radiation model for remote alpine areas, Theoretical and Applied Climatology, 27(2-3): 159-187, doi: 10.1007/BF02243741.

Marks, D., J. Domingo, D. Susong, T. Link, and D. Garen. 1999. A spatially distributed energy balance snowmelt model for application in mountain basins, Hydrological Processes, 13(12-13): 1935-1959, doi: 10.1002/(SICI)1099-1085(199909)13:12/13<1935::AID-HYP868>3.0.CO;2-C.

Martinec, J. and A. Rango. 1981. Areal distribution of snow water equivalent evaluated by snow cover monitoring, Water Resources Research, 17(5): 1480-1488, doi: 10.1029/WR017i005p01480.

Maurer, E.P., I.T. Stewart, C. Bonfils, P.B. Duffy, and D. Cayan. 2007. Detection, attribution, and sensitivity of trends toward earlier streamflow in the Sierra Nevada, Journal of Geophysical Research, 112(D11): D11118, doi: 10.1029/2006JD008088.

Milly, P.C.D., J. Betancourt, M. Falkenmark, R.M. Hirsch, Z.W. Kundzewicz, D.P. Lettenmaier, and R.J. Stouffer. 2008. Climate change - Stationarity is dead: Whither water management?, Science, 319(5863): 573-574, doi: 10.1126/science.1151915.

Molotch, N.P. and S.A. Margulis. 2008. Estimating the distribution of snow water equivalent using remotely sensed snow cover data and a spatially distributed snowmelt model: A multi-resolution, multi-sensor comparison, Advances in Water Resources, 31(11): 1503-1514, doi: 10.1016/j.advwatres.2008.07.017.

Mote, P.W., A.F. Hamlet, M.P. Clark, and D.P. Lettenmaier. 2005. Declining mountain snowpack in western North America, Bulletin of the American Meteorological Society, 86(1): 39-49, doi: 10.1175/BAMS-86-1-39.

NOAA/NWS (2011), California Nevada River Forecast Center http://www.cnrfc.noaa.gov/.

Olyphant, G.A. 1984. Insolation topoclimates and potential ablation in alpine snow accumulation basins: Front Range, Colorado, Water Resources Research, 20(4): 491-498, doi: 10.1029/WR020i004p00491.

Painter, T.H., K. Rittger, C. McKenzie, P. Slaughter, R.E. Davis, and J. Dozier. 2009. Retrieval of subpixel snow covered area, grain size, and albedo from MODIS, Remote Sensing of Environment, 113(4): 868-879, doi: 10.1016/j.rse.2009.01.001.

Seager, R., M.F. Ting, I. Held, Y. Kushnir, J. Lu, G. Vecchi, H.P. Huang, N. Harnik, A. Leetmaa, N.C. Lau, C.H. Li, J. Velez, and N. Naik. 2007. Model projections of an imminent transition to a more arid climate in southwestern North America, Science, 316(5828): 1181-1184, doi: 10.1126/Science.1139601.

Wan, Z. and J. Dozier. 1996. A generalized split-window algorithm for retrieving land-surface temperature from space, IEEE Transactions on Geoscience and Remote Sensing, 34(4): 892-905, doi: 10.1109/36.508406.